

Physics-Informed Neural Networks for Solving Contact Problems in Three Dimensions

Tarik Sahin^[0000-0002-4134-3726],
Daniel Wolff^[0000-0001-5767-7803] and
Alexander Popp^[0000-0002-8820-466X]

Abstract This paper explores the application of physics-informed neural networks (PINNs) to tackle forward problems in 3D contact mechanics, focusing on small deformation elasticity. We utilize a mixed-variable formulation, enhanced with output transformations, to enforce Dirichlet and Neumann boundary conditions as hard constraints. The inherent inequality constraints in contact mechanics, particularly the Karush-Kuhn-Tucker (KKT) conditions, are addressed as soft constraints by integrating them into the network's loss function. To enforce the KKT conditions, we leverage the nonlinear complementarity problem (NCP) approach, specifically using the Fischer-Burmeister function, which is known for its advantageous properties in optimization. We investigate two benchmark examples of PINNs in 3D contact mechanics: a single contact patch test and the Hertzian contact problem.

1 Introduction

Machine learning methods often demand large datasets, which are challenging to obtain in engineering due to costly experiments, the unavailability of certain measurements (e.g., inaccessible components or the absence of suitable sensors), or long simulation runtimes. When real-world data is available, it is frequently noisy or mislabeled. These limitations can undermine the performance of classical data-driven

Tarik Sahin
University of the Bundeswehr Munich, Institute for Mathematics and Computer-Based Simulation (IMCS), e-mail: tarik.sahin@unibw.de

Daniel Wolff
University of the Bundeswehr Munich, Institute for Mathematics and Computer-Based Simulation (IMCS) e-mail: d.wolff@unibw.de

Alexander Popp
University of the Bundeswehr Munich, Institute for Mathematics and Computer-Based Simulation (IMCS) e-mail: alexander.popp@unibw.de

models, as they lack a physics-based mechanism to validate predictions. Physics-informed neural networks (PINNs) have been introduced to address these challenges [1].

Using automatic differentiation, PINNs integrate physical knowledge (e.g., partial differential equations (PDEs)) into the neural network’s loss function, introducing physics-based regularization that mitigates the black-box nature of purely data-driven approaches. For forward problems, PINNs serve as mesh-free PDE solvers, requiring only sampling points from the (arbitrary, potentially geometrically intricate) domain [2]. They also overcome the curse of dimensionality when approximating high-dimensional functions [3] and excel in solving inverse problems by seamlessly incorporating measurement data [4]. PINNs can be also used for thermo-mechanical coupling problems using a mixed formulation [5].

In this work, we extend PINNs to 3D contact mechanics, building on previous 2D examples [6]. The employed PINNs are developed based on a mixed-variable formulation inspired by the Hellinger-Reissner principle, where both displacement and stress fields are network outputs. Contact mechanics involves Karush-Kuhn-Tucker (KKT) type constraints, commonly referred to as Hertz-Signorini-Moreau conditions, which we incorporate as soft constraints using the Fischer-Burmeister nonlinear complementarity problem (NCP) function. This approach efficiently handles inequality constraints in contact mechanics. We validate the method with two examples assuming small deformation elasticity for simplicity: (1) a single contact patch test where all points are in contact and (2) the Hertzian contact problem, where the contact area is detected as part of the solution.

2 Problem Formulation: Contact Mechanics

We consider a 3D contact problem between an elastic body and a fixed rigid obstacle, as illustrated in Fig. 1. In the reference configuration, the elastic body is denoted by Ω_0 , while in the current configuration, it is represented by Ω_t . The rigid obstacle remains fixed in its configuration, Ω_r . Fig. 1c illustrates a scenario where the two bodies are in contact. The surface of the elastic body can be divided into three regions: the Dirichlet boundary $\partial\Omega_u$, where displacements are specified; the Neumann boundary $\partial\Omega_\sigma$, where tractions are applied; and the potential contact boundary $\partial\Omega_c$, where contact constraints may apply. The true contact surface is a subset of $\partial\Omega_c$ and is determined as part of the solution procedure.

We define the target boundary value problem (BVP) as follows:

$$\nabla \cdot \boldsymbol{\sigma} + \hat{\mathbf{b}} = \mathbf{0} \quad \text{in } \Omega_t, \quad (1)$$

$$\mathbf{u} = \hat{\mathbf{u}} \quad \text{on } \partial\Omega_u, \quad (2)$$

$$\boldsymbol{\sigma} \cdot \mathbf{n} = \hat{\mathbf{t}} \quad \text{on } \partial\Omega_\sigma. \quad (3)$$

In this formulation, $\boldsymbol{\sigma}$ is the Cauchy stress tensor, and \mathbf{u} is the displacement vector, which is the primary unknown. The vector $\hat{\mathbf{b}}$ represents body forces acting on the

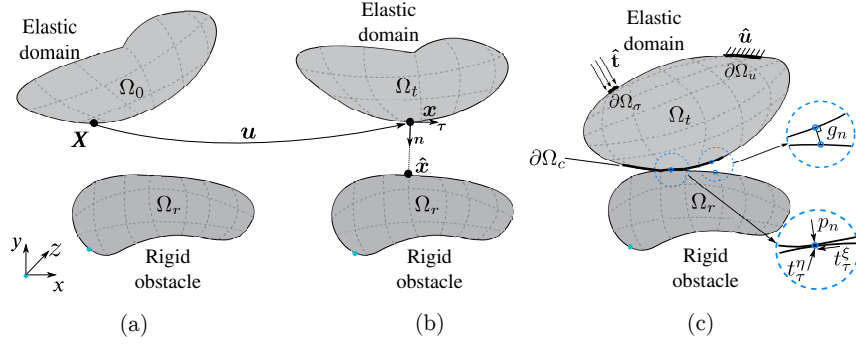


Fig. 1 Contact problem between an elastic body and a rigid obstacle. (a) Reference configuration, (b) current configuration, (c) boundary conditions illustration, including the gap g_n , tangential tractions t_τ^ξ , t_τ^η and contact pressure p_n .

domain, and \mathbf{n} is the outward unit normal vector on the boundary. Displacements prescribed on the Dirichlet boundary $\partial\Omega_u$ are denoted by $\hat{\mathbf{u}}$, while tractions prescribed on the Neumann boundary $\partial\Omega_\sigma$ are represented by $\hat{\mathbf{t}}$.

In addition to these equilibrium equations, we also account for the kinematic and constitutive equations that describe the behavior of the elastic material. For simplicity, linear kinematics and linear-elastic material behavior will be assumed in the numerical examples section, given by:

$$\boldsymbol{\varepsilon} = \frac{1}{2}(\boldsymbol{\nabla}\mathbf{u} + \boldsymbol{\nabla}\mathbf{u}^T), \quad (4)$$

$$\boldsymbol{\sigma} = \mathbb{C} : \boldsymbol{\varepsilon}. \quad (5)$$

Here, $\boldsymbol{\varepsilon}$ is the infinitesimal strain tensor, and \mathbb{C} is the fourth-order elasticity tensor.

For the case of linear isotropic elasticity, the constitutive equation can be simplified using Hooke's law:

$$\boldsymbol{\sigma} = \lambda \text{tr}(\boldsymbol{\varepsilon})\mathbf{I} + 2\mu\boldsymbol{\varepsilon}, \quad (6)$$

where λ and μ are the Lamé parameters, $\text{tr}(\cdot)$ denotes the trace operator (sum of diagonal components), and \mathbf{I} is the identity tensor.

The displacement vector \mathbf{u} of the elastic body is determined by describing the motion of a point in the reference configuration $\mathbf{X} \in \Omega_0$ to a point in the current configuration $\mathbf{x} \in \Omega_t$, as shown in Figs. 1a and 1b. This relation is expressed as follows:

$$\mathbf{u} = \mathbf{x} - \mathbf{X}. \quad (7)$$

The gap function g_n , which measures the separation between the elastic and rigid bodies in the current configuration, is defined as:

$$g_n = -\mathbf{n} \cdot (\mathbf{x} - \hat{\mathbf{x}}). \quad (8)$$

Here, $\hat{\mathbf{x}}$ denotes the closest point projection of \mathbf{x} onto the surface of Ω_r (see Fig. 1b). Since all contact constraints are enforced in the current configuration, the contact pressure p_n , and tangential traction components t_τ^ξ and t_τ^η and are obtained by decomposing the contact traction vector \mathbf{t}_c via traction vector decomposition (TVD) as follows:

$$\mathbf{t}_c = p_n \mathbf{n} + t_\tau^\xi \boldsymbol{\tau}^\xi + t_\tau^\eta \boldsymbol{\tau}^\eta, \quad p_n = \mathbf{t}_c \cdot \mathbf{n}, \quad t_\tau^\xi = \mathbf{t}_c \cdot \boldsymbol{\tau}^\xi, \quad t_\tau^\eta = \mathbf{t}_c \cdot \boldsymbol{\tau}^\eta, \quad (9)$$

where

$$\mathbf{t}_c = \boldsymbol{\sigma} \cdot \mathbf{n} \quad \text{on } \partial\Omega_c. \quad (10)$$

For a frictionless contact problem, the classical Karush-Kuhn-Tucker (KKT) type constraints (Eq. 11), also known as the Hertz-Signorini-Moreau (HSM) conditions, are employed along with the frictionless sliding conditions (Eq. 12):

$$g_n \geq 0, \quad p_n \leq 0, \quad p_n g_n = 0, \quad (11)$$

$$t_\tau^\xi = 0, \quad t_\tau^\eta = 0. \quad (12)$$

For further details on more advanced contact constitutive laws, including friction, the reader is referred to [7, 8].

In this study, we adopt a mixed-variable approach, where both the displacement field \mathbf{u} and the stress tensor $\boldsymbol{\sigma}$ are treated as primary variables for solving contact problems. An additional key requirement is the stress-to-stress coupling between the primary variable $\boldsymbol{\sigma}$ and the secondary variable $\boldsymbol{\sigma}''$, defined by the relation

$$\boldsymbol{\sigma} = \boldsymbol{\sigma}'' . \quad (13)$$

The term $\boldsymbol{\sigma}''$ is computed by inserting the kinematic equation (Eq. 4) into the constitutive law (Eq. 5). This condition ensures that the two master fields remain consistent and compatible throughout the solution process. This method has been comprehensively discussed in the work by Sahin et al. [6].

3 Extending Physics-Informed Neural Networks for 3D Contact Mechanics

3.1 Loss Formulation in PINNs

In quasi-static solid mechanics using PINNs, a fully-connected neural network (FNN) \mathcal{N} with parameters $\boldsymbol{\theta}$ and spatial coordinates \mathbf{x} to the displacement \mathbf{u} and stress tensor $\boldsymbol{\sigma}$:

$$\tilde{\mathbf{u}} = \mathcal{N}_u(\mathbf{x}; \boldsymbol{\theta})', \quad \tilde{\boldsymbol{\sigma}} = \mathcal{N}_\sigma(\mathbf{x}; \boldsymbol{\theta})'. \quad (14)$$

Here, $(\cdot)'$ denotes a user-defined output transformation and (\cdot) indicates a predicted quantity. It is important to note that, due to the conservation of angular momentum, $\boldsymbol{\sigma} = \boldsymbol{\sigma}^T$, only 6 stress components are predicted instead of 9.

The total loss \mathcal{L}_E for the boundary value problem (without contact) in the mixed-variable formulation, with additional experimental data, is given by:

$$\mathcal{L}_E = \mathcal{L}_{\text{PDEs}} + \mathcal{L}_{\text{DBC}s} + \mathcal{L}_{\text{NBC}s} + \mathcal{L}_{\text{EXP}s}, \quad (15)$$

where:

$$\begin{aligned} \mathcal{L}_{\text{PDEs}} = & \sum_{i_n=1}^{N_m} w_{i_n} \frac{1}{N_{rp}} \sum_{i_{rp}=1}^{N_{rp}} \left[[\nabla \cdot \tilde{\boldsymbol{\sigma}}(\mathbf{x}^{i_{rp}}) + \hat{\mathbf{b}}(\mathbf{x}^{i_{rp}})]_{i_n} \right]^2 \\ & + \sum_{i_n=N_m+1}^{N_n} w_{i_n} \frac{1}{N_{rp}} \sum_{i_{rp}=1}^{N_{rp}} \left[[\tilde{\boldsymbol{\sigma}}(\mathbf{x}^{i_{rp}}) - \mathbb{C} : \tilde{\boldsymbol{\varepsilon}}(\mathbf{x}^{i_{rp}})]_{i_n} \right]^2, \end{aligned} \quad (16)$$

$$\mathcal{L}_{\text{DBC}s} = \sum_{i_{bc,D}=1}^{N_{bc,D}} w_{i_{bc,D}} \frac{1}{N_{bp,D}} \sum_{i_{bp,D}=1}^{N_{bp,D}} \left[\tilde{\mathbf{u}}(\mathbf{x}^{i_{bp,D}}) - \hat{\mathbf{u}}(\mathbf{x}^{i_{bp,D}}) \right]_{i_{bc,D}}^2, \quad (17)$$

$$\mathcal{L}_{\text{NBC}s} = \sum_{i_{bc,N}=1}^{N_{bc,N}} w_{i_{bc,N}} \frac{1}{N_{bp,N}} \sum_{i_{bp,N}=1}^{N_{bp,N}} \left[\tilde{\boldsymbol{\sigma}}(\mathbf{x}^{i_{bp,N}}) \cdot \mathbf{n} - \hat{\mathbf{t}}(\mathbf{x}^{i_{bp,N}}) \right]_{i_{bc,N}}^2, \quad (18)$$

$$\begin{aligned} \mathcal{L}_{\text{EXP}s} = & \sum_{i_{e,u}=1}^{N_{e,u}} w_{i_{e,u}} \frac{1}{N_{ep,u}} \sum_{i_{ep,u}=1}^{N_{ep,u}} \left[\tilde{\mathbf{u}}(\mathbf{x}^{i_{ep,u}}) - \mathbf{u}^*(\mathbf{x}^{i_{ep,u}}) \right]_{i_{e,u}}^2 \\ & + \sum_{i_{e,\sigma}=1}^{N_{e,\sigma}} w_{i_{e,\sigma}} \frac{1}{N_{ep,\sigma}} \sum_{i_{ep,\sigma}=1}^{N_{ep,\sigma}} \left[\tilde{\boldsymbol{\sigma}}(\mathbf{x}^{i_{ep,\sigma}}) - \boldsymbol{\sigma}^*(\mathbf{x}^{i_{ep,\sigma}}) \right]_{i_{e,\sigma}}^2. \end{aligned} \quad (19)$$

Here, $(\cdot)^*$ denotes measurements. The terms $\mathcal{L}_{\text{DBC}s}$ and $\mathcal{L}_{\text{NBC}s}$ represent the loss contributions from Dirichlet and Neumann boundary conditions, respectively, while $\mathcal{L}_{\text{EXP}s}$ accounts for losses due to additional experimental data. In the mixed-variable formulation, $\mathcal{L}_{\text{PDEs}}$ is composed of two parts: the balance equation (Eq. 1) and the stress-to-stress coupling (Eq. 13). The index N_m distinguishes between the loss weights for balance equation and stress-to-stress coupling. The terms $\{w_{i_n}\}_{i_n=1}^{N_n}$, $\{w_{i_{bc}}\}_{i_{bc}=1}^{N_{bc}}$ and $\{w_{i_e}\}_{i_e=1}^{N_e}$ denote the loss weights for the individual components of $\mathcal{L}_{\text{PDEs}}$, $\mathcal{L}_{\text{BC}s}$, $\mathcal{L}_{\text{EXP}s}$, respectively. For a detailed explanation, we refer to [6]. Since stress components are directly predicted by the network, Neumann BCs can be imposed as hard constraints using an output transformation. Moreover, only first-order derivatives of the network outputs are needed, as the governing equations in this formulation involve exclusively first-order derivatives.

For the problem formulation with contact, the total loss function \mathcal{L}_C is defined as:

$$\mathcal{L}_C = \mathcal{L}_E + \mathcal{L}_{\text{FS}} + \mathcal{L}_{\text{KKT}}, \quad (20)$$

where \mathcal{L}_{FS} enforces the frictionless sliding conditions (Eq. 12) on the contact surface $\partial\Omega_c$:

$$\mathcal{L}_{\text{FS}} = w_{\text{fs},\xi} |t_{\tau}^{\xi}|_{\partial\Omega_c} + w_{\text{fs},\eta} |t_{\tau}^{\eta}|_{\partial\Omega_c}. \quad (21)$$

Here, $w_{\text{fs},\xi}$ and $w_{\text{fs},\eta}$ represent the loss weights corresponding frictionless sliding conditions and $|\cdot|$ denotes the mean squared error (MSE), calculated as $\frac{1}{n} \sum_{i=1}^n (\cdot)^2$. While the evaluation of the normal gap g_n is a topic of intense discussion in the context of discretization methods such as the finite element method [8], it is consistently expressed by evaluating the orthogonal projection of the elastic body onto the rigid flat surface. Additionally, \mathcal{L}_{KKT} comprises the Karush-Kuhn-Tucker conditions and will be introduced in the next section.

3.2 Enforcing the Karush-Kuhn-Tucker Inequality Constraints: the Fischer-Burmeister NCP Function

Nonlinear complementarity problem (NCP) functions reformulate inequalities as equalities. A common NCP function is the Fischer-Burmeister function [9], defined as

$$\phi_{\text{FB}}(a, b) := a + b - \sqrt{a^2 + b^2} = 0 \iff a \geq 0, b \geq 0, ab = 0. \quad (22)$$

By setting $a = \tilde{g}_n$ and $b = -\tilde{p}_n$, the Fischer-Burmeister function gives the KKT loss:

$$\mathcal{L}_{\text{KKT}} = w_{\text{KKT}} \left| \tilde{g}_n - \tilde{p}_n - \sqrt{\tilde{g}_n^2 + \tilde{p}_n^2} \right|_{\partial\Omega_c}, \quad (23)$$

where, w_{KKT} denotes the loss weight. The Fischer-Burmeister function is ideal for mean squared error (MSE) loss calculations because $(\phi_{\text{FB}})^2$ is continuously differentiable at $a = b = 0$. This method simplifies optimization and parameter tuning by requiring only one loss weight instead of one per condition.

4 Numerical Examples

The numerical examples share the following common settings. The PINN takes spatial coordinates $\mathbf{x} = (x, y, z)$ as inputs and maps them to transformed mixed-form outputs $(\tilde{\mathbf{u}}, \tilde{\boldsymbol{\sigma}})$. The networks are initialized using the *Glorot uniform* initializer, and the activation function is set to *tanh*. Training begins with the *Adam* optimizer at a learning rate of $lr = 0.001$ for 2000 epochs, followed by the *L-BFGS-B* optimizer until the solver converges. Additionally, body forces are omitted. Unless otherwise specified, all loss weights are set to 1.

4.1 Single Contact Patch Test

In the first example, we examine a single patch contact test as depicted in Fig. 2a. An elastic cube is subjected to external pressure on its top surface. The geometry is constrained in the x -direction at $x = 0$ and in the z -direction at $z = 0$. The analytical solution, as derived from [10], is given by:

$$u_x = \nu \frac{p}{E} x, \quad u_y = -\frac{p}{E} y, \quad u_z = \nu \frac{p}{E} z, \quad \sigma_{yy} = -p.$$

For this setup, the parameters are $E = 1.33$, $\nu = 0.33$, $p = 0.1$, and $l = h = w = 1$.

We use the following output transformation to impose the Dirichlet and Neumann boundary conditions (BCs) shown in Fig. 2b as hard constraints:

$$\begin{aligned} \tilde{u}_x &= x \mathcal{N}_{u_x}, & \tilde{u}_z &= z \mathcal{N}_{u_z}, & \tilde{\sigma}_{xx} &= (l-x) \mathcal{N}_{\sigma_{xx}}, \\ \tilde{\sigma}_{yy} &= -p + (h-y) \mathcal{N}_{\sigma_{yy}}, & \tilde{\sigma}_{zz} &= (w-z) \mathcal{N}_{\sigma_{zz}}, & \tilde{\sigma}_{xy} &= x(h-y)(l-x) \mathcal{N}_{\sigma_{xy}}, \\ \tilde{\sigma}_{yz} &= z(h-y)(w-z) \mathcal{N}_{\sigma_{yz}}, & \tilde{\sigma}_{xz} &= xz(l-x)(w-z) \mathcal{N}_{\sigma_{xz}}. \end{aligned}$$

This transformation enforces the Dirichlet and Neumann BCs as hard constraints, while the contact conditions are treated as soft constraints, as described earlier. Additionally, the employed PINN is a fully connected neural network consisting of 5 hidden layers with 50 neurons each.

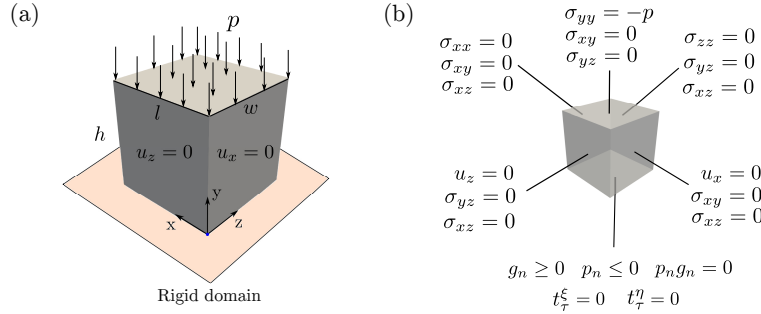


Fig. 2 Single patch contact test problem: (a) geometry, constraints, and loading, (b) all relevant boundary conditions.

The comparison between the predicted and analytical solutions for the single contact patch test is shown in Fig. 2. The results are only provided for the displacement components u_x and u_y , as the behavior of u_z is identical to that of u_x . Both predicted displacement fields exhibit a linear distribution that closely matches the analytical solution. While the contact constraints are imposed softly, the displacement component u_y approaches zero near the contact surface, reflecting the expected behavior. Thanks to the output transformation, the boundary conditions at $x = 0$ and $z = 0$ are enforced as hard constraints, ensuring that the corresponding displacement

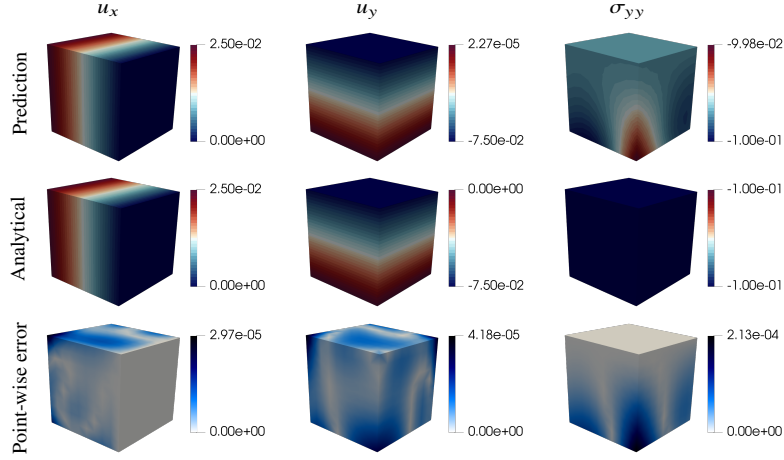


Fig. 3 Comparison of the PINN predictions and the analytical solution for the single contact patch test. Point-wise error is defined as $E_{abs}^* = \text{abs}(\tilde{*} - *)$.

components are strictly zero. This accuracy is further supported by point-wise error analysis, which confirms the close agreement between predictions and the analytical solution. Similarly, the normal stress component in the y -direction, σ_{yy} , remains close to the expected value of -0.1 across the entire domain, consistently aligning with the analytical solution.

4.2 Hertzian Contact Problem

In the second example, we consider a finite linear elastic half-cylinder ($E = 200$ and $\nu = 0.3$) lying on a rigid flat domain under a uniform pressure $p = 0.5$ as depicted in Fig. 4a. Additionally, we set the height of the quarter cylinder to $w = 1$ and the radius as $R = 1$. See Appendix 1 for the analytical solution.

Similar to the previous example, the following output transformation is applied to impose the Dirichlet and Neumann boundary conditions (BCs) shown in Fig. 4b as hard constraints:

$$\begin{aligned} \tilde{u}_x &= \frac{x}{E} \mathcal{N}_{u_x}, \quad \tilde{u}_y = \frac{1}{E} \mathcal{N}_{u_y}, \quad \tilde{u}_z = \frac{z(w+z)}{E} \mathcal{N}_{u_z}, \quad \tilde{\sigma}_{yy} = -p + (-y) \mathcal{N}_{\sigma_{yy}}, \\ \tilde{\sigma}_{xy} &= xy \mathcal{N}_{\sigma_{xy}}, \quad \tilde{\sigma}_{yz} = (w+z)zy \mathcal{N}_{\sigma_{yz}}, \quad \tilde{\sigma}_{xz} = (w+z)zx \mathcal{N}_{\sigma_{xz}}. \end{aligned}$$

This output transformation ensures that the DBCs and NBCs on the flat surfaces are strictly enforced. To simplify the optimization process, the displacements are scaled using the inverse of the Young's modulus. Moreover, NBCs on the curved surface are enforced using soft constraints due to the coupling between the normal and shear

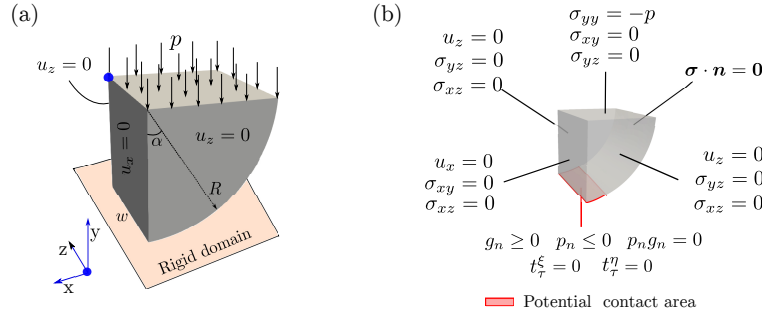


Fig. 4 The Hertzian contact problem between an elastic quarter-cylinder and a rigid flat domain: (a) geometry, constraints, loading using the symmetry, (b) all relevant boundary conditions.

stress components on those surfaces. To define the potential contact area, we set $\alpha = 15^\circ$ and enforce the contact constraints exclusively on the points lying on that surface (highlighted in red in Fig 4b).

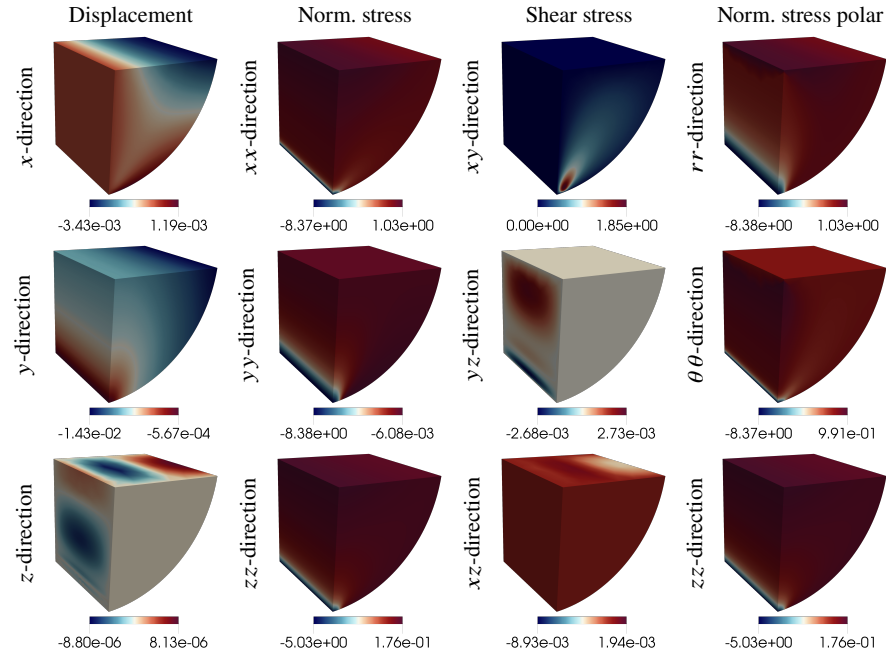


Fig. 5 The data-enhanced PINN predictions for the Hertzian contact example. Polar components are computed based on the cylindrical coordinates.

In the following, we investigate two distinct PINN application cases for the Hertzian contact problem. In the first case, we deploy a PINN as pure PDE solver (denoted as "plain vanilla PINN"), and in the second case, we deploy a data-enhanced

PINN including additional data obtained from the analytical solution (see Eqs. 24-26 provided in Appendix 1). In total 150 additional data points are selected along three distinct lines (each involves 50 points) located at $z = -1$, $z = -0.5$, $z = 0$. Each line starts at $y = -1$ and ends at $y = -0.7642$. Furthermore, the loss weight for the KKT term in Eq. 23 is set to $w_{\text{KKT}} = 500$, ensuring that the PINN model prioritizes learning the contact constraints. The same neural network architecture as in the previous example is utilized.

The PINN predictions for the Hertzian contact example with data enhancement are provided in Fig. 5. These results include the displacement fields and stress fields in both normal and shear directions. Additionally, the normal components of the stress tensor are presented in cylindrical coordinates. It can be observed that the employed output transformation explicitly enforces components of the displacement and stress fields on the target surfaces, such as $u_z = 0$ and $\sigma_{yy} = -0.5$. Furthermore, the maximum pressure reaches $\sigma_{rr} = 8.38$, which is very close to the maximum analytical pressure $p_{\text{max}} = 8.36$ (Eq. 27). Additionally, see Appendix 3 for the predictions of the plain vanilla PINN.

A comparison between the PINN predictions and the analytical solution for both the plain vanilla and data-enhanced PINNs is presented in Fig. 6. While the plain vanilla PINN underpredicts the analytical solution particularly in regions with higher nonlinearity, the data-enhanced PINN demonstrates superior performance, aligning closely with the analytical solution. This can be verified by the relative L_2 errors as provided in Table 1 (see Appendix 2). For instance, $E_{L_2}^{\sigma_{yy}}$ is computed as 5.29% for the plain vanilla PINN, whereas it is significantly reduced to 0.17% for the data-enhanced PINN, highlighting the impact of data enhancement. Note that the predictions are evaluated using unseen data points at the line $z = -0.75$ to demonstrate the model's ability to generalize.

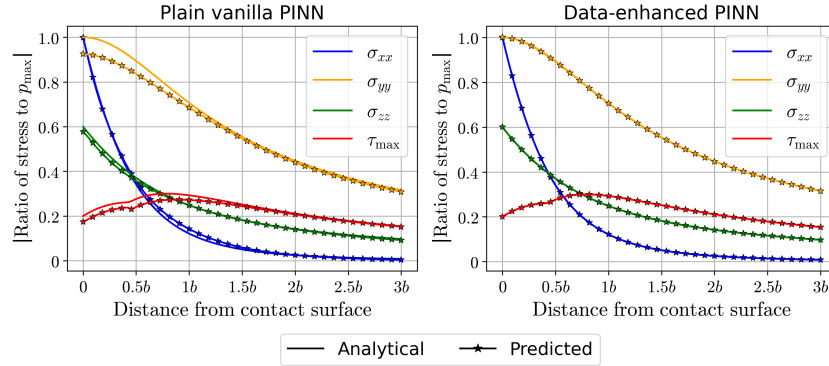


Fig. 6 Comparison of the predictions with the analytical solution for the Hertzian contact problem using the plain vanilla PINN and data-enhanced PINN.

5 Conclusion

In this study, we have introduced an extension of physics-informed neural networks (PINNs) for solving 3D forward problems in contact mechanics under the assumption of linear elasticity. The proposed framework has been evaluated on two benchmark examples: the single contact patch test and the Hertzian contact problem. Results were validated using existing analytical solutions. To enforce the inequality constraints inherent to contact problems, a nonlinear complementarity problem (NCP) function, specifically the Fischer-Burmeister function, was employed. We conclude that enhancing PINNs with additional measurement data can significantly improve the training performance. This leads to hybrid models that effectively leverage both the underlying physics and data-driven insights, resulting in improved accuracy and robustness.

Acknowledgements This research paper is funded by dtec.bw - Digitalization and Technology Research Center of the Bundeswehr under the project RISK.twin. dtec.bw is funded by the European Union—NextGenerationEU.

Competing Interests The authors have no conflicts of interest to declare that are relevant to the content of this chapter.

Appendix 1

The analytical solution for the Hertzian contact problem between a cylinder and a plane rigid surface is expressed as [11]

$$\sigma_{xx} = -p_{\max} \left(\frac{1 + 2\frac{y^2}{b^2}}{\sqrt{1 + \frac{y^2}{b^2}}} - 2\left|\frac{y}{b}\right| \right), \quad (24)$$

$$\sigma_{yy} = \frac{-p_{\max}}{\sqrt{1 + \frac{y^2}{b^2}}}, \quad (25)$$

$$\sigma_{zz} = -2\nu p_{\max} \left(\sqrt{1 + \frac{y^2}{b^2}} - \left|\frac{y}{b}\right| \right), \quad (26)$$

where

$$p_{\max} = \frac{2F}{\pi bw}, \quad b = \sqrt{\frac{2F(1-\nu^2)/E}{\pi w \cdot 1/(2R)}}, \quad F = 2Rwp. \quad (27)$$

By inserting $p = 0.5$, $R = 1$, $w = 1$, $\nu = 0.3$ and $E = 200$, the area of contact, which is a narrow rectangle, i.e. bw , can be calculated, leading to $b = 0.076$, and the maximum pressure is computed as $p_{\max} = 8.36$. Additionally, the maximum shear stress can be expressed as

$$\tau_{\max} = \frac{\sigma_{zz} - \sigma_{yy}}{2} \quad \text{for } 0 \leq y \leq 0.436b, \quad (28)$$

$$\tau_{\max} = \frac{\sigma_{xx} - \sigma_{yy}}{2} \quad \text{for } y \geq 0.436b. \quad (29)$$

The analytical solutions can be easily computed based on the vertical distance from the contact zone y .

Appendix 2

	$E_{L_2}^{\sigma_{xx}}$	$E_{L_2}^{\sigma_{yy}}$	$E_{L_2}^{\sigma_{zz}}$	$E_{L_2}^{\tau_{\max}}$
Plain vanilla PINN	3.81	5.29	3.31	7.41
Data-enhanced PINN	0.15	0.17	0.16	0.18

Table 1 Comparison of relative L_2 errors (%) between the predictions and the analytical solution for the plain vanilla PINN and the data-enhanced PINN.

Appendix 3

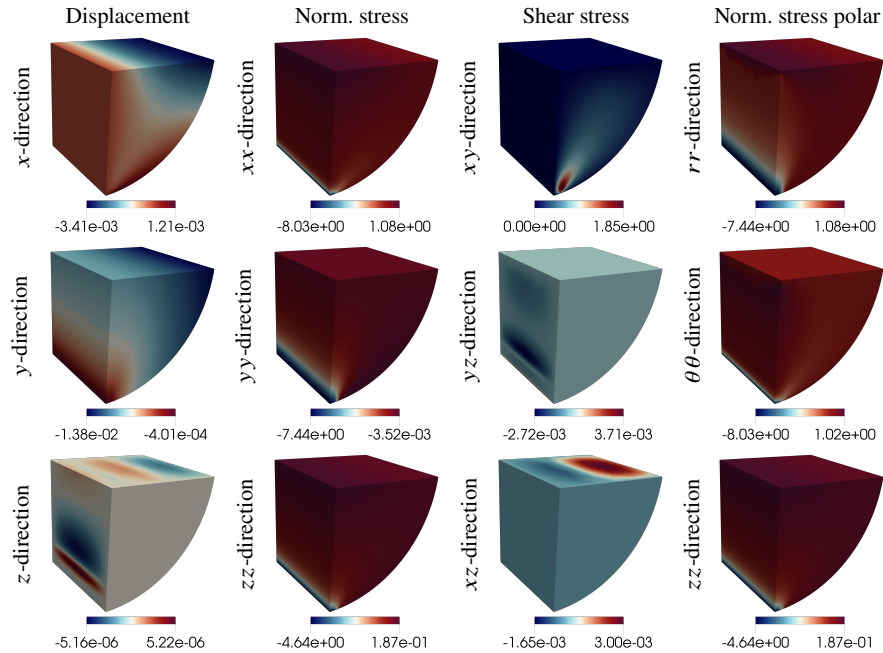


Fig. 7 The predictions of the plain vanilla PINN for the Hertzian contact example. Polar components are computed based on the cylindrical coordinates.

References

1. Raissi, M., Perdikaris, P., & Karniadakis, G. (2019). Physics-informed neural networks: A deep learning framework for solving forward and inverse problems involving nonlinear partial differential equations. *Journal of Computational Physics*, 378, 686–707. <https://doi.org/10.1016/j.jcp.2018.10.045>
2. Arend Torres, F., Negri, M., Nagy-Huber, M., Samarin, M., & Roth, V. (2022). Mesh-free Eulerian physics-informed neural networks. *arXiv preprint arXiv:2204.13469*. <https://arxiv.org/abs/2204.13469>
3. Poggio, T., Mhaskar, H., Rosasco, L., Miranda, B., & Liao, Q. (2017). Why and when can deep-but not shallow-networks avoid the curse of dimensionality: A review. *International Journal of Automation and Computing*, 14(5), 503–519. <https://doi.org/10.1007/s11633-017-1054-2>
4. Sahin, T., Wolff, D., Danwitz, M., & Popp, A. (2024). Towards a hybrid digital twin: Fusing sensor information and physics in surrogate modeling of a reinforced concrete beam. *2024 Sensor Data Fusion: Trends, Solutions, Applications (SDF)*, 1–8. <https://doi.org/10.1109/SDF2024.1234567>

5. Harandi, A., Moeineddin, A., Kaliske, M., Reese, S., & Rezaei, S. (2024). Mixed formulation of physics-informed neural networks for thermo-mechanically coupled systems and heterogeneous domains. *International Journal for Numerical Methods in Engineering*, 125(3), e7388. <https://doi.org/10.1002/nme.7388>
6. Sahin, T., von Danwitz, M., & Popp, A. (2024). Solving forward and inverse problems of contact mechanics using physics-informed neural networks. *Advanced Modeling and Simulation in Engineering Sciences*, 11, 11. <https://doi.org/10.1186/s40323-024-00211-7>
7. Popp, A., & Wriggers, P. (Eds.). (2018). *Contact modeling for solids and particles* (Vol. 585). Springer International Publishing. ISBN: 978-3-319-90154-1. <https://doi.org/10.1007/978-3-319-90155-8>
8. Wriggers, P., & Laursen, T. A. (2006). *Computational contact mechanics* (2nd ed.). Springer. <https://doi.org/10.1007/978-3-540-32609-0>
9. Fischer, A. (1992). A special Newton-type optimization method. *Optimization*, 24(3), 269–284. <https://doi.org/10.1080/02331939208843875>
10. Timoshenko, S., & Goodier, J. (1951). *Theory of elasticity*. McGraw-Hill.
11. Budynas, R., & Nisbett, J. (2014). *Shigley's mechanical engineering design* (10th ed.). McGraw-Hill Education.